Imaging the deep cerebellar nuclei: A probabilistic atlas and normalization procedure

J. Diedrichsen [a,b,*], S. Maderwald [c,d], M. Küper [e], M. Thürling [c,e], K. Rabe [c,e], E.R. Gizewski [c,d,f], M.E. Ladd [c,d], D. Timmann [e]

[a] Institute of Cognitive Neuroscience, University College London, UK
[b] School of Psychology, Adeilad Brigantia University of Wales, Bangor, UK
[c] Erwin L. Hahn Institute for Magnetic Resonance Imaging, University Duisburg-Essen, Essen, Germany
[d] Department of Diagnostic and Interventional Radiology and Neuroradiology, University Duisburg-Essen, Essen, Germany
[e] Department of Neurology, University of Duisburg-Essen, Essen, Germany
[f] Department of Neuroradiology, University of Giessen, Giessen, Germany

ABSTRACT

The deep cerebellar nuclei (DCN) are a key element of the cortico-cerebellar loop. Because of their small size and functional diversity, it is difficult to study them using magnetic resonance imaging (MRI). To overcome these difficulties, we present here three related methodological advances. First, we used susceptibility-weighted imaging (SWI) at a high-field strength (7 T) to identify the dentate, globose, emboliform and fastigial nucleus in 23 human participants. Due to their high iron content, the DCN are visible as hypo-intensities. Secondly, we generated probabilistic maps of the deep cerebellar nuclei in MNI space using a number of common normalization techniques. These maps can serve as a guide to the average location of the DCN, and are integrated into an existing probabilistic atlas of the human cerebellum (Diedrichsen et al., 2009). The maps also quantify the variability of the anatomical location of the deep cerebellar nuclei after normalization. Our results indicate that existing normalization techniques do not provide satisfactory overlap to analyze the functional specialization within the DCN. We therefore thirdly propose a ROI-driven normalization technique that utilizes both information from a T1-weighted image and the hypo-intensity from a T2*-weighted or SWI image to ensure overlap of the nuclei. These techniques will promote the study of the functional specialization of subregions of the DCN using MRI.

© 2010 Elsevier Inc. All rights reserved.

Introduction

A key anatomical feature of the cerebellum is the deep cerebellar nuclei (DCN), which relay all output from the cerebellar cortex to cortical and subcortical targets. The fastigial nuclei receive the output from the vermis, the interposed nuclei (in humans comprised of the emboliform and globose nuclei) from the paravermis, and the large dentate nuclei from the lateral cerebellar hemispheres.

For studies of human participants with focal lesions it is therefore very important to know, whether and to what degree the DCN are involved. Furthermore, while most functional neuroimaging studies focus on the cerebellar cortex (for a review see: Stoodley and Schmahmann, 2009), the BOLD signal here mostly reflects the input to the cerebellum (Thomsen et al., 2009). Therefore, reliable measurement of activity in the DCN, which should relate more to the cerebellar output, could provide useful functional insights. Indeed, a number of studies have provided evidence that reliable functional activation within the dentate nucleus can be observed (Dimitrova et al., 2006a; Habas, 2009; Kim et al., 1994).

The small size of the cerebellar nuclei poses a challenge for human MRI studies. While the size of the dentate nucleus in itself is substantial ($\sim 13 \times 19 \times 14$ mm^3), one has to keep in mind that it is composed of a number of subdivisions with unique functions. In the monkey, the dorso-rostral part of the dentate is relaying somatotopic organized output to the motor cortex, while the ventro-caudal part provides outputs to the parietal (area 7b) and prefrontal cortices (Dum and Strick, 2003; Middleton and Strick, 1997). Thus, the functional subdivisions of the dentate nuclei, as well as the interposed and fastigial nuclei are very small. This causes problems for traditional MRI group analyses. For example, it has been shown that after normalization to the MNI152 template, the dentate nucleus overlaps maximally only for 71% of the participants, with the average overlap being substantially poorer (Dimitrova et al., 2006b). Thus, with common normalization methods the chance that functionally corresponding areas of the deep cerebellar nuclei superimpose across participants is quite small.

An additional challenge for functional imaging of the deep cerebellar nuclei is posed by the high iron content of the DCN, which leads to signal losses due to magnetic susceptibility artifacts

* Corresponding author. Institute of Cognitive Neuroscience, University College London, Alexandra House, 17 Queen Square, London WC1N 3AR, UK.
E-mail address: j.diedrichsen@ucl.ac.uk (J. Diedrichsen).
URL: http://www.icn.ucl.ac.uk/motorcontrol (J. Diedrichsen).

(Aoki et al., 1989; Gans, 1924; Maschke et al., 2004). For T2*-weighted EPI sequences, the mean signal of voxels in the deep cerebellar nuclei is typically only 2/3 of the surrounding white and 1/2 of the adjacent gray matter. This is problematic, as both functional activations and noise in fMRI data scale roughly proportional with the mean voxel signal (Diedrichsen and Shadmehr, 2005), meaning that the functional signal from the deep cerebellar nucleus is quite small compared to the surrounding noise signals. When one now applies a 6–10 mm smoothing kernel to account for poor overlap across participants, a small functional signal is averaged with much more variable signal from the surrounding tissue. This makes it likely that true activations of individual compartments of the DCN are missed (Type I error). Furthermore, there is a substantial danger that reported activations of the DCN may be due to activation from surrounding gray matter structures (Type II error).

To address these shortcomings we provide here three related improvements. First, we used ultrahigh (7 T) MRI to collect anatomical data of the cerebellar nuclei in the submillimeter range (Gizewski et al., 2007). We used a susceptibility-weighted imaging sequence (Haacke et al., 2009; Haacke et al., 2004), which is very sensitive to the high iron content of the DCN, allowing us to identify the dentate, interposed, and fastigial nucleus in most participants. This technique will be useful to determine the disruption of the DCN for individual patients with focal cerebellar lesions.

Secondly, we provide a probabilistic atlas of the location of the nuclei in a common atlas space. Because probabilistic maps are dependent on the normalization method that is used to bring individual brains into a common reference frame (Diedrichsen, 2006), we systematically compared a number of normalization techniques. Older, yet still commonly-used normalization techniques, are outperformed substantially by more modern techniques such as concurrent segmentation and normalization (Ashburner and Friston, 2005) or cerebellar-only normalization (SUIT, Diedrichsen, 2006). The resulting maps allow for the valid assignment of structural impairment and functional activations to specific cerebellar nuclei, and have been integrated into an existing probabilistic atlas of the human cerebellum (Diedrichsen et al., 2009).

The evaluated anatomical normalization methods all rely on T1-weighted images, on which the deep cerebellar nuclei are not visible. Assuming that the surrounding structures are brought into perfect alignment through normalization, the variability of the nuclei after normalization therefore provides a quantitative measure of the anatomical variability of the location of the cerebellar nuclei in relationship to these surrounding structures. This remaining variability, however, poses a problem when trying to study the functional specialization of different compartments of the DCN.

We therefore thirdly propose a new technique for the group analysis of functional data from the deep cerebellar nuclei. This method incorporates the information from the hypo-intensity of the dentate nucleus, a piece of information that is readily available from a standard T2*-weighted image (such as the mean EPI image), into the normalization process. This effectively ensures near perfect superposition of the dentate nuclei across different participants, thereby eliminating the remaining anatomical variability. The approach combines the high anatomical accuracy of ROI-based analyses with the ease and information richness of map-wise comparisons. The normalization routines are made freely available online as an addendum to the cerebellar normalization toolbox (Diedrichsen, 2006).

Methods

Subjects

MR images were collected in 28 healthy participants. Five subjects were excluded, because of movement artifacts (n = 3) or incidental finding of MRI abnormalities (n = 2: cerebellar cavernoma, large subarachnoidal cyst in the posterior fossa). The final analysis included data from 23 subjects (9 males, 14 females; mean age 35.1, SD 13.1 years, 21–61 years). All subjects except three were right-handed: one subject was left-handed and two were ambidextrous based on the Edinburgh handedness inventory (Oldfield, 1971). The study was approved by the local ethics committee. All subjects gave informed written and oral consent.

MRI scanning

Susceptibility-weighted imaging (SWI) was performed with a whole-body 7 T MR scanner (Magnetom 7 T, Siemens Healthcare, Erlangen, Germany), and an eight-channel transmit/receive head coil (Rapid Biomed, Würzburg, Germany). Isotropic voxel size of the T2*-weighted SWI was $0.5 \times 0.5 \times 0.5$ mm^3 (TR/TE = 35/16.9 ms, FOV 224×182 mm^2, flip 19°, BW 160 Hz/pixel, 144 slices, matrix 448×364, slice thickness 0.5 mm, Grappa R = 2 and TA 16:14 min). In SWI, magnetic susceptibility caused by high iron content is visible both in the raw magnitude and phase images. To remove slow-varying phase changes caused by the global geometry of the distortion of the main field, the phase images were high-pass filtered. A phase mask is then multiplied with the magnitude images to create SWI images (Haacke et al., 2009; Haacke et al., 2004).

In addition, we acquired 3D T1-weighted image, using a magnetization prepared rapid acquisition gradient echo (MPRAGE) sequence, TR/TE = 2700/3.71 ms, FOV = 256×256 mm^2, flip 7°, BW 200 Hz/pixel; 224 slices; matrix 256×256, slice thickness 1 mm, voxel size = $1 \times 1 \times 1$ mm^3, Grappa R = 2 and TA = 6:49 min.
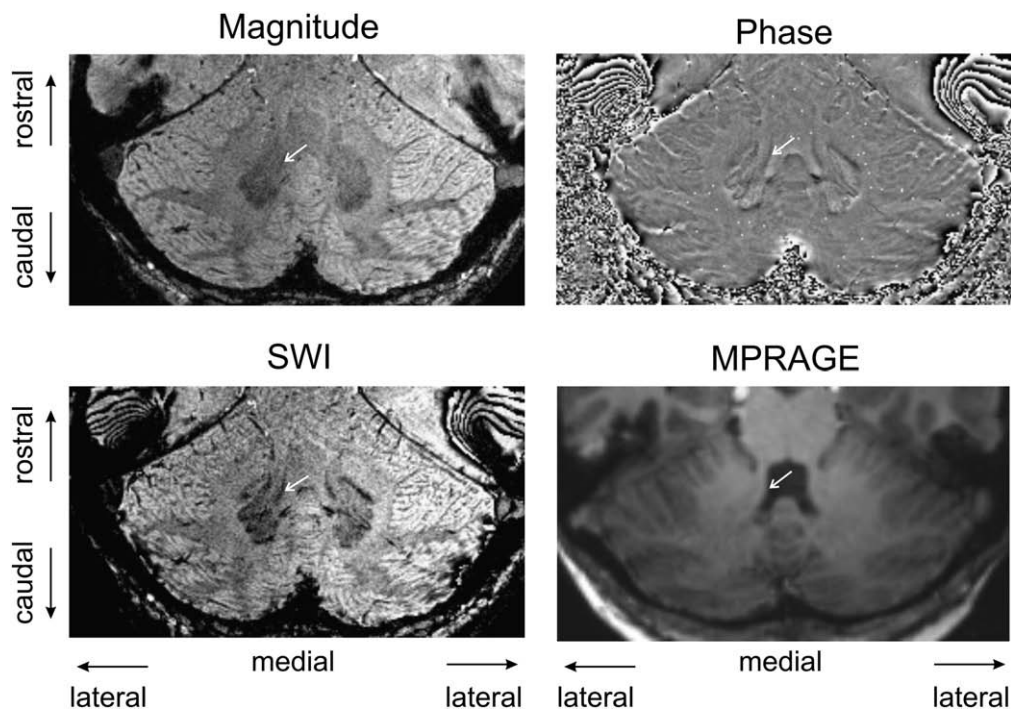
Identification of cerebellar nuclei

Directions in space were labeled according to Dum and Strick (2003). The horizontal plane was defined approximately according to the AC–PC line. In the horizontal plane, the anterior direction is labeled rostral and the posterior direction caudal. In the coronal plane, the superior direction is referred to as dorsal and the inferior direction as ventral.

Cerebellar nuclei were visually identified on the high-pass filtered phase images. Due to the phase-shift caused by the magnetic susceptibility of the tissue, boundaries between areas of relatively low and high iron content appeared as a bright signal in these images. The cerebellar nuclei were then marked manually as regions of interest (ROIs) using MRICro software (Rorden, 2007) on the phase images: we started in the horizontal plane, and subsequently refined the ROI drawing using the coronal and parasagittal sections. Drawing was performed by a trained lab technician under close supervision of one of the senior authors (DT). Finally, the ROIs were examined and refined on the SWI images, which showed the DCN as hypo-intensities (Fig. 1).

For cross-validation, a second rater (KR) repeated the drawing of the ROIs on 9 of the individual brains. The correspondence scores (analogous to a correlation) were calculated for each ROI as follows: we divided the number of voxels marked by both raters, by the square-root of the number of voxels marked by rater 1 times the number of voxels marked by rater 2.

Nuclei were identified based on their known localization in the anatomical literature (Jakob, 1928; Voogd, 2004) and by comparison with available 3D histological atlases of the cerebellum (Angevine et al., 1961; Duvernoy, 1995; Schmahmann et al., 2000). The large dentate nucleus is easily identified based on its characteristic shape: it is shaped like a sac with corrugated thin walls, which has been compared with a "dry (cavernous) plum" (Jakob, 1928) and a "crumpled purse" (Chan-Palay, 1977). The opening of the dentate nucleus is called the hilus and is directed rostrally and ventromedially.

Fig. 1. Identification of cerebellar nuclei on susceptibility-weighted images. The DCN are visible as hypo-intensities in the magnitude image, but are more clearly outlined in the high-pass filtered phase image. These images also show the folding of the dentate nucleus. In the SWI images, these two pieces of information are combined. In comparison, no information about the location of the nuclei is apparent in a T1-weighted MPRAGE scan. The arrow denotes the border of the fourth ventricle.

The ROI drawing followed the corrugated wall of the dentate nucleus as good as possible.

The interposed nuclei, which consist of the emboliform and globose nuclei in humans, are slightly harder to identify. The emboliform nucleus resides next to the neck of the dorsal hilus of the dentate nucleus (Larsell and Jansen, 1972), and is bordered medially by the globose nucleus. The main body of the emboliform nucleus is located more dorso-rostrally than the main part of the globose nucleus (Jansen and Brodal, 1958; Larsell and Jansen, 1972; Voogd, 2004). The emboliform nucleus tapers more caudally, where it becomes difficult to differentiate from the major bulk of the globose nucleus. The globose nucleus, on the other hand, has a rostral stalk-like extension consisting of numerous smaller cell groups. While the main parts of the emboliform and globose nuclei were always clearly separated, it was not always possible to clearly identify the smaller, fractionated parts. For further analysis we therefore combined the data from both nuclei into a common ROI, labeled interposed nucleus in accordance with the animal literature.

The most medial of the deep cerebellar nuclei, the fastigial nucleus, could again be reliably identified in most participants. This nucleus is located next to the midline bordering the roof of the fourth ventricle.

The volumes and the maximal extensions in the three planes and volume of each nucleus were calculated and compared to data based on histological findings (Blinkov and Glezer, 1968; Kozlova, 1984).

Generation of probabilistic atlas

The ROIs were drawn to capture the individual folding patterns of the DCN. For the probabilistic atlas we were interested in how well the location of the nuclei, rather than single folds, superimposed across individuals. Therefore we slightly smoothed (1.5 mm FWHM) the ROI images and then binarized them to 0/1. The threshold was picked such that the extent of the ROI in x, y and z directions did not change through the smoothing and thresholding operations. Thus, the resulting images contained the outline of the deep cerebellar nuclei independent of their exact folding structure.

These ROIs were then normalized using 4 different procedures. (1) Nonlinear normalization to the MNI152 template, as implemented in SPM2/SPM5/SPM8 (Friston et al., 1999), using default parameters. (2) Nonlinear MNI normalization with concurrent segmentation as implemented in SPM5/8 (Ashburner and Friston, 2005). (3) SUIT normalization based on the T1-weighted images only (Diedrichsen, 2006). (4) SUIT normalization based on the T1-weighted image and the ROI obtained from a T2*-weighted image (see next section).

We used three measures to compare the quality of overlap of the normalized dentate, interposed and fastigial ROIs in the different atlas spaces. First, we determined the voxel with the maximal overlap and took the percentage of participants for which this voxel was within the nucleus' ROI as the measure of best overlap. We also calculated the mean overlap averaged over all voxels in the atlas space that fell within the ROI from at least one participant. Finally, as a quantitative measure of spatial spread of the normalized nuclei, we determined the center of gravity for each individual ROI in atlas space. We then computed the volume of the ellipsoid that contained 95% of these centers by calculating the 3 principal axes of the cloud formed by these points. The volume of the confidence ellipsoid was then calculated from the eigenvalues corresponding to these axes.

ROI-based SUIT normalization

To improve the overlap of the deep cerebellar nuclei for group analysis of functional data, we developed a new normalization technique. The algorithm is based on the previous SUIT normalization algorithm (Diedrichsen, 2006), but also utilizes the bean-shaped hypo-intensity visible on T2*-weighted scans, which indicates the location of the dentate (and possibly part of the interposed) nuclei. We outlined this hypo-intensity on the magnitude image of the SWI scan as a rough "Hull" ROI. In contrast to the dentate ROI that was used for the generation of the atlas, this ROI did not try to follow the wall of the dentate, but simply marked the main body of the dentate nucleus. This rough Hull ROI can also readily be obtained from T2- or T2*-weighted scans with standard resolution and field strength. In other

work (Küper et al., submitted for publication) we have used a ROI drawn on the mean EPI image acquired at 1.5 T with good success.

To generate a spatially representative atlas template in SUIT space, we first transferred all individual Hull ROIs into the atlas space, using the deformation calculated based in the standard SUIT normalization (T1-weighted scan only). We then averaged the ROI images in the atlas space and applied a threshold such that the volume of the resulting area matched the average volume of individual Hull ROIs in atlas space. The result is a representative template of the position and extent of the bean-shaped hypo-intensity in atlas space. Note that this template image is separate from the probabilistic atlas and is only used for the spatial normalization.

The normalization procedure then attempts to match simultaneously the T1-weighted image of the individual to the high-resolution SUIT template and the individual Hull ROI to the template Hull ROI. While it would be theoretically possible to only use the ROI information, such normalization is not satisfactory. For example, for rotation around the x-axis, the shape of the dentate does not provide enough information to lead to a well-defined solution. Information about the surrounding tissue needs to be used as additional constraint. Furthermore, the integration has the advantage that the same normalization then can be used for both dentate and cerebellar cortical activity.

In the current version of the software, this multimodal normalization is achieved by creating a weighted image that sets the brightness of the Hull ROI 4 times higher than the 90th percentile of the brightness of the T1 scan. This combination is performed both on the original image and the template. The combined image is then normalized to the combined template by nonlinear image matching. In our experiences the weight of the ROI relative to the anatomical image does not influence the normalization much, the current value was chosen as it ensured good overlap of the dentate nucleus.

Results

Individual anatomy

The dentate nuclei could be identified in all of the 23 subjects. The interposed nucleus was identified in 21 subjects, and fastigial nuclei in 17 subjects. Fig. 2 shows three horizontal slices of an individual SWI image, on which the nuclei are visible as hypo-intensities. For direct comparison we superimposed the ROI drawings for the individual nuclei on the same slices in a second row. In the most ventral slice (a) the dentate nucleus (D; indicated in red) with its corrugated thin walls and the medial hilus is clearly visible. In the second slice (b), the

ventral parts of the interposed nucleus come into the field of view, which most likely represent predominantly the globose nucleus (G; green). In the last slice (c) the more dorsal parts of the interposed nuclei are seen, consisting mainly of the emboliform nucleus (E; yellow). In the roof of the 4th ventricle, two small hypo-intensities indicate the location of the fastigial nuclei (F; blue).

To establish inter-rater reliability in the identification of the nuclei, a second rater marked the four ROIs again on 9 of the 23 individual brains. The gross overlap was very good: the difference in mean location of the ROIs between raters was 0.66 mm (std = 0.43 mm). Even on a voxel-by-voxel level the agreement was satisfactory, with correspondence scores (see Methods) ranging between 0.4 and 0.73 (mean = 0.59, SD = 0.092).

The general pattern of localization of the deep cerebellar nuclei was consistent across subjects. In most cases it was possible to identify the main body of the emboliform nucleus lying more dorsal and rostral and the main cluster of the globose nucleus more caudal. However, it was most often not possible to separate the nuclei with certainty. In particular, it was difficult to separate the ventro-caudal extent of the emboliform nucleus from the bulk of the globose nucleus. Furthermore, because the emboliform nucleus is known to be continuous with the dorsomedial parts of the dentate nucleus in places (Larsell and Jansen, 1972) separation of dentate and emboliform nucleus was not always possible with certainty. Finally, because of its fractionated nature, more dorsal parts of the globose nucleus were likely missed in some cases. Differences in local iron distribution may have contributed. The iron staining of the fastigial, globose and emboliform nucleus has been described to be the same as for the dorsomedial parts of the dentate nucleus (Jakob, 1928), which is not as strong as for the ventrolateral parts of the dentate. Because of this relatively high uncertainty, we decided to combine the globose and emboliform nucleus into a common ROI for the generation of the probabilistic atlas.

Average volumes and extent

The average volume and the average extent in the medial–lateral (x, width), posterior–anterior (y, length) and inferior–superior (z, height) dimensions as measured in the individual anatomical scans can be seen in Table 1. To validate our results, we compared these measurements for all deep cerebellar nuclei with histological data from human post-mortem studies. The largest anatomical series to date (Kozlova, 1984) is based on 100 cerebellar preparations (age range 22–72 years). The histological sections had a thickness of 0.5 mm, the same as the spatial resolution in the present study.
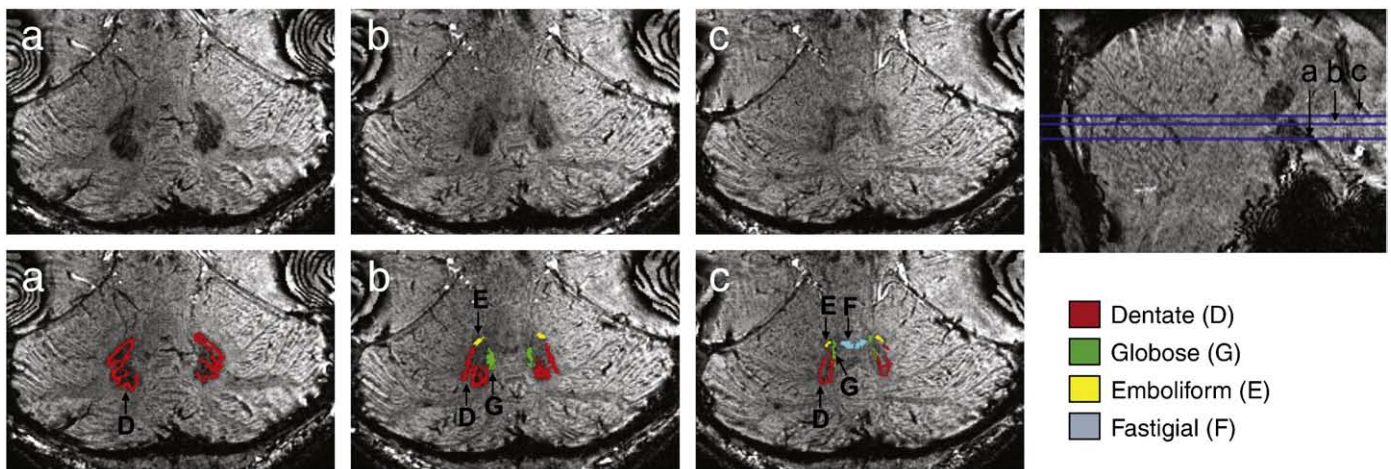

Fig. 2. ROI drawing of the deep cerebellar nuclei in an individual on the susceptibility-weighted image (7 T, 0.5 mm isotropic resolution). Three horizontal slices are shown without (upper row) and with (lower row) ROIs displayed.

Table 1

Volumes and extent (between-person SD) of the deep cerebellar nuclei. The data of our MRI study are compared with histological findings based on 100 preparations (Kozlova, 1984).

	Present data				Kozlova, 1984	
	Left		Right			
Dentate					**Dentate**	
Volume (mm³)	362.8	(89.2)	366.1	(85.2)	n.a.	n.a.
x-extent (mm)	13.0	(1.1)	13.0	(1.2)	13.80	(2.01)
y-extent (mm)	19.4	(1.3)	19.2	(1.2)	18.21	(2.30)
z-extent (mm)	14.2	(1.6)	14.4	(1.3)	13.90	(2.01)
Interposed					**Emboliform/globose**	
Volume (mm³)	35.9	(14.2)	36.1	(11.4)	n.a.	n.a.
x-extent (mm)	4.6	(1.3)	4.6	(1.2)	4.75/1.63	(0.87/0.73)
y-extent (mm)	8.9	(1.3)	9.3	(1.6)	7.75/3.29	(1.64/1.04)
z-extent (mm)	7.7	(1.2)	8.0	(1.2)	3.58/2.65	(1.11/0.86)
Fastigii					**Fastigii**	
Volume (mm³)	9.2	(5.9)	8.2	(5.2)	n.a.	n.a.
x-extent (mm)	3.0	(0.8)	2.7	(0.6)	4.37	(0.52)
y-extent (mm)	2.9	(0.9)	2.6	(0.8)	4.88	(0.82)
z-extent (mm)	2.3	(1.0)	2.4	(1.0)	2.60	(0.84)

For the dentate nucleus, the authors report an average extent of $13.8 \times 13.9 \times 18.2$ mm, which lies within the confidence bounds of the values found in our MRI study. This suggests that labeling through SWI scans outlines the dentate nucleus without any major losses. In terms of the volume, our measures for the dentate nucleus of 366 mm³ are much smaller than for previous MRI studies (900 mm³ in Deoni and Catani, 2007; 840 mm³ in Dimitrova et al., 2002), but still nearly twice the size compared to histological estimates (155 mm³ in Höpker, 1951). These differences are likely caused by partial volume effects (see Discussion).

The width (x) of the combined interposed nuclei is determined dorsally mostly by the width of the emboliform nucleus, and ventrally mostly by the width of the globose nucleus. Therefore, the width of the interposed nucleus should roughly match the width of the wider nucleus. This was also the case: Kozlova gives a width of 4.75 mm for the emboliform nucleus, which matches the width of the interposed ROI in our study. Likewise, the size of the interposed nucleus in the rostro-caudal (y) direction was smaller than the sum of the histological values for the emboliform and globose nucleus. Only in the dorso-ventral (z) direction, was the extent of our combined interposed ROI slightly larger than the sum of the nuclei in the histological study.

For the fastigial nucleus we found an average extent of 2.8 (width) × 2.7 (length) × 2.3 (height) mm. The z-extent matches the average height reported in the study by Kozlova (1984), but the mean x- and y-extent were smaller than the histological estimates. Other anatomical studies also report the size of the fastigial nucleus to be approximately 4–6 mm in width, 3–10 mm in length, and 2–5 mm in height (Dejerine, 1901; Heimburger and Whitlock, 1965; Jakob, 1928; Jansen and Brodal, 1958). Thus, it is possible that the MRI images did not allow for the identification of the whole fastigial nucleus, but that we underestimated especially the medial–lateral extent of the nucleus.

Paired t-tests were used to compare the extent and the volume for the right and left cerebellar nuclei. In contrast to a previous study (Deoni and Catani, 2007), no left–right asymmetry in the volume of the dentate nucleus was found, $t(22) = -0.608$, $p = 0.549$. Also, the x-, y- and z-extent were not significantly different between the left and right sides (all p values > 0.336). Likewise, comparing volumes and extent of the interposed and fastigial nuclei showed no significant right–left difference (all p values > 0.23).

Finally, there was no significant correlation between age and volumes of the dentate (spearman rank correlation, $r = -0.359$, $p = .093$) or the fastigial nucleus ($r = 0.146$, $p = .562$). Only for the

interposed nucleus, the correlation between age and volume reached significance ($r = -0.516$, $p = 0.017$).

Overlap of nuclei

The spatial spread of the deep cerebellar nuclei across different individuals after normalization is caused by two factors. First, there is anatomical variability of the position, orientation and size of the nuclei in relationship to the surrounding cerebellar landmarks. Secondly, depending on the normalization method used, the surrounding landmarks may not have been brought into full registration.

Consistent with previous reports (Dimitrova et al., 2006b) we found very poor overlap of the dentate nuclei when using standard whole-brain MNI normalization. The maximal overlap was 77% and the mean overlap only 23% (Table 2, Fig. 3). To determine the spread of the nuclei, we calculated the center of mass for individual nuclei in the atlas space and determined the ellipsoid that contained 95% of these nuclei (see Methods). In case of the standard SPM normalization, these confidence bounds contained a substantial volume (Table 2), with the highest variability in the z-direction (SD = 4.6 mm) and lower variability in the y- (SD = 2.8 mm) and x-directions (SD = 2.1).

The maximal overlap of the dentate nuclei increased to 93% when using the segmentation (SPM5) algorithm and to 94% when using the SUIT normalization, and the mean overlap increased to 32% and 33%, respectively. Concomitantly, the spatial spread of the nuclei was reduced by nearly a factor of 10 (Table 2, Fig. 3). The two normalization methods differed little form each other.

Both methods rely on T1-weighted images and therefore have only information about the surrounding anatomical landmarks, but not about the DCN. We have previously shown that SUIT normalization leads to a 75% overlap of individual gray matter lobule, compared to 67% for the segmentation algorithm (Diedrichsen et al., 2009). This improvement did not lead to a better alignment for the nuclei. Thus, it is likely that the surrounding structures are superimposed nearly as well as possible and that the residual spatial spread of the nuclei is mainly caused by true anatomical variability of how the dentate nucleus is situated in relationship to these landmarks visible on a T1 scan. We can therefore assume that a spatial standard deviation of 1.3–1.5 mm of each of the spatial direction is a fairly good estimate of the true anatomical variability of the location of the dentate nucleus in respect to the surrounding structures. Very similar measures are obtained for the variability of the interposed and fastigial nuclei.

Table 2

Overlap and variability of the deep cerebellar nuclei under different normalization algorithms. The maximal overlap denotes the best overlap of participants. Mean overlap is the average number of overlapping participants for all voxels that contained the ROI of one participant or more. The volume of spatial spread denotes the volume of the ellipsoid that holds ~95% of the center of masses of individual nuclei.

	Dentate	Interposed	Fastigial
Maximal overlap (%)			
SPM normalization	77.0	55.6	24.8
SPM segmentation	93.3	73.4	24.8
SUIT	94.0	79.0	29.7
SUIT + ROI	100.0	92.7	48.1
Mean overlap (%)			
SPM normalization	23.4	14.6	8.7
SPM segmentation	32.8	20.8	10.4
SUIT	33.7	21.7	11.6
SUIT + ROI	47.5	25.0	15.5
Volume of spatial spread of COM (mm³)			
SPM normalization	635.5	415.3	152.4
SPM segmentation	62.8	50.9	44.4
SUIT	73.1	58.8	35.9
SUIT + ROI	3.2	23.1	18.9
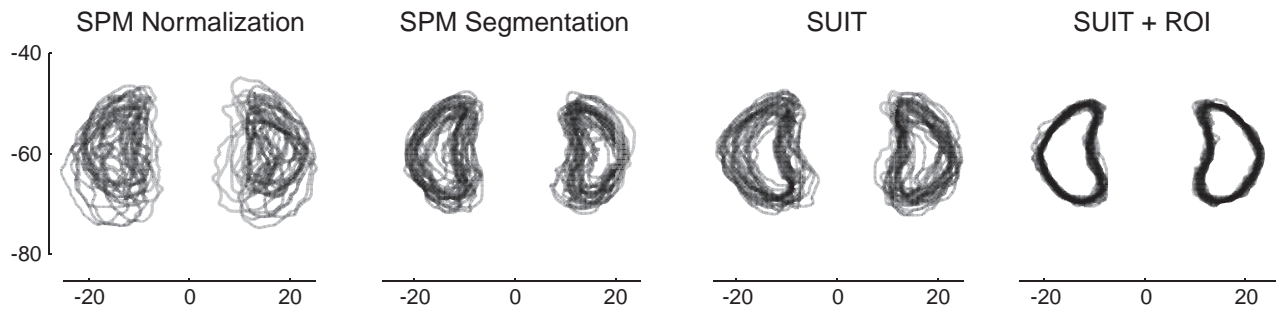
Fig. 3. Overlap of the dentate nucleus using different normalization methods. The outlines of the dentate nucleus from 23 participants in MNI space are shown. Standard SPM normalization to the MNI 152 template (left) resulted in the poorest overlap. Segmentation + normalization, as well as SUIT normalization (middle) led to substantial improvements. Near perfect overlap of the nuclear structures can be achieved by incorporating the hypo-density information from a standard T2* image into the normalization process (SUIT + ROI, right). Horizontal sections at z = −37 (z = −43 for SPM normalization to account for the spatial bias) are shown, and all spatial scale are given MNI coordinates (mm).

Probabilistic atlas and summary map

From the overlap maps after SUIT normalization, SPM normalization, and SPM segmentation we generated the probabilistic maps. These maps provide a probability measure for every voxel of how likely that voxel belonged to each of the specific ROIs across individuals.

We also generated a summary map that shows for every voxel the most likely nucleus it belonged to. We thresholded each probability map, such that the extent in the x-, y-, and z-direction (averaged) matched the average extent found in individual subjects. For this calculation we took into account that the MNI152 template is slightly larger than the average brain (in our sample 8% in x-, and 17% in z-direction, amounting to a volume increase of 27%). After accounting for these enlargements, the summary map (Fig. 4) represents validly the average position, arrangement, and extent of the DCN in individual anatomies (Fig. 2).

It should be noted, however, that the summary map does not necessarily preserve the average volume and shape. The average volumes of individual ROIs after normalization into atlas space were 1380 mm^3 for the dentate, 160 mm^3 for the interposed and 13 mm^3

Fig. 4. 3D-reconstruction of the probabilistic atlas of the deep cerebellar nuclei in SUIT space. The probability density of the dentate nucleus (red), the interposed nucleus (green) and the fastigial nucleus (blue) are shown. The threshold (dentate: 0.28, interposed: 0.29, and fastigial: 0.20) is set such that the extent of the resulting surfaces matched the average extent of the nuclei in individual subjects.
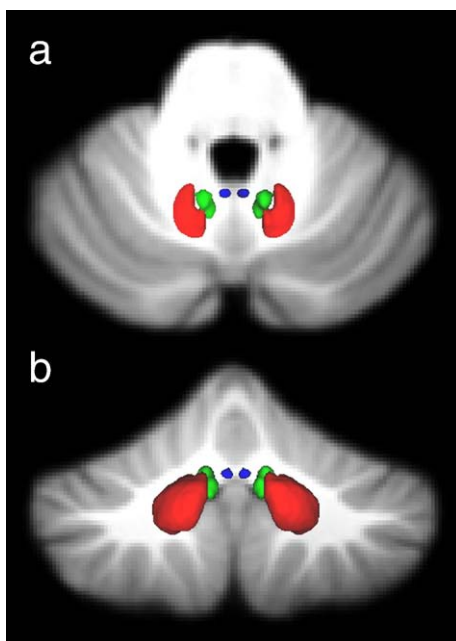
for the fastigial nucleus. The increase in volume compared to the ROIs in individual space is caused by the smoothing and thresholding operations, which lead small gaps to be filled in. In contrast, the summary map volumes were 1944 mm^3 for the dentate, 184 mm^3 for the interposed and 12 mm^3 for the fastigial nuclei. This enlargement is caused by further filling-in through averaging and thresholding. Only for the more spherically shaped fastigial nucleus, the volume was roughly preserved.

ROI-driven normalization

The probabilistic maps provide a valuable guide to the average location of the nuclei in atlas space. However, they also allow us to assess the remaining anatomical variability of the nuclei, which, given the small size of the functional subregions of the dentate nucleus or the medial nuclei, would severely reduce the power of fMRI group analyses. To achieve a better overlap, multimodal information needs to be utilized for normalization. For the SUIT + ROI normalization method, we used a rough bean-shaped ROI drawing from the SWI-weighted scans to enforce the accurate overlap of all individual dentate nuclei. This was clearly successful in our sample (Fig. 3, right); the mean overlap for the dentate nucleus increased to 47.5%, and the spread volume reduced dramatically (see Table 2). Thus, our method can ensure that equivalent parts of the dentate nucleus overlap for group analyses of functional data. The overlap of the dentate nucleus indirectly also improved the overlap of the neighboring interposed and fastigial nuclei, which were not explicitly used in the normalization algorithm. The spatial spread for these nuclei decreased by a factor of 1.9 and 2.5 respectively (see Table 2). Thus, the relative spatial arrangement of the nuclei appears to be stable across participants, and information of the localization of the dentate nucleus can improve the overlap of neighboring nuclei.

Discussion

In sum, the paper provides a number of innovations that will be useful for the study of the deep cerebellar nuclei in humans. First, we showed the feasibility of depicting the deep cerebellar nuclei using susceptibility-weighted imaging in high-field MRI (7 T). This technique is useful for detecting the deep cerebellar nuclei in single participants for detailed patient and functional imaging studies. Secondly, we provide a probabilistic atlas for the nuclei in the standard atlas space of the MNI template for different normalization methods. This atlas, which is integrated in an already existing atlas of the lobular anatomy (Diedrichsen et al., 2009), provides a guide to interpret functional data of groups of individuals. Finally, we propose a new normalization method that further improves the

overlap of the dentate nucleus and that can be applied to functional imaging data without further image acquisition.

Visualizing deep cerebellar nuclei using susceptibility-weighted imaging

Here we show the feasibility of using high-field (7 T) MRI to visualize the deep cerebellar nuclei in humans in the submillimeter range. Advantages compared to our previous studies using 1.5 T MRI (Dimitrova et al., 2002; Dimitrova et al., 2006b) were manifold.

First, spatial resolution was improved nearly by a factor of 12 (0.5 mm isotropic voxel size compared to $1.15 \times 0.86 \times 1.5$ mm^3). Second, good quality images were obtained with no need of averaging. Third, different cerebellar nuclei were reliably visible even in young (18–30 years) subjects. Because the iron content increases with age, we often failed to see the nuclei in younger subjects at 1.5 T (Maschke et al., 2004).

Using the SWI sequence, we could visualize the corrugated walls of the dentate nucleus and the localization of the hilus (Fig. 1). The walls of the dentate nucleus, however, were not always continuous, especially in the most dorsal parts. This may be caused by differences in local iron contribution. Iron staining has been reported to be stronger in the ventrolateral, macrogyric parts than in the dorsomedial, microgyric parts of the dentate nucleus (Gans, 1924; Guizzetti, 1915; Jakob, 1928). Despite these limitations, the extent of the dentate nucleus matched well with that reported in previous literature (Blinkov and Glezer, 1968; Heimburger and Whitlock, 1965; Jakob, 1928; Jansen and Brodal, 1958; Kozlova, 1984). Thus, we are fairly confident that the SWI was able to reveal the main parts of the dentate nucleus in most participants.

In contrast to the well-matching spatial extent, the volumes of the dentate ROIs were nearly twice the size of those reported in the histological literature. Here, mean volumes of roughly 155 mm^3 for a single dentate nucleus are commonly reported (Höpker, 1951). Although shrinkage artifacts may lead to underestimation of the volumes in the living brain (Angevine et al., 1961), the main reason for this difference lies most likely in the spatial resolution of MRI and the resulting partial volume effects. The thickness of a single cell layer of the dentate nucleus varies between 0.3 mm and 0.5 mm (Jansen and Brodal, 1958). In order to show single cell layers, an isotropic voxel size of 0.25 mm would therefore be required. However, our isotropic resolution of 0.5 mm already constitutes a step forward compared to previous studies, which used roughly 1 mm resolution data (Deoni and Catani, 2007; Dimitrova et al., 2002). These studies reported average dentate volumes of 840 mm^3 (Dimitrova et al., 2002) and 900 mm^3 (Deoni and Catani, 2007), about five times the size suggested by histological estimates. In sum, our results indicate that volume estimates of the dentate nucleus from MRI studies need to be treated with caution, as such estimates will depend on the spatial resolution, the local iron content, and the technique employed to determine the ROI boundary.

Despite good accuracy in estimating the extent of the dentate nucleus, the use of SWI to visualize the deep cerebellar nucleus has certain limitations. For example we were unable to subdivide the emboliform and globose nuclei with certainty in most cases. Furthermore, the comparison with histological data indicates that we have underestimated the medial–lateral extent of the fastigial nucleus in most participants. The smaller size of these nuclei compared to the dentate nucleus makes MRI investigations challenging. More importantly, the iron concentration in these nuclei is not as high as in the ventral dentate (Jakob, 1928). However, this is the first time that we have been able to determine the location of the smaller cerebellar nuclei in a group of participants. To date, this has been only achieved using averages of a number of MRI scans of a single individual (Deoni and Catani, 2007; Dimitrova et al., 2002).

These developments will allow us to use the SWI sequence to determine in individual patients whether focal cerebellar lesions encompass the dentate nucleus, or the smaller interposed and fastigial nuclei. Because the nuclei constitute the only output of the cerebellar cortex, a small lesion in the nucleus may result in similar deficits as a much larger lesion in the cerebellar cortex. Therefore, it is very important for lesion-symptom mapping (Timmann et al., 2008), to be able to estimate the exact involvement of the nuclei.

Possible alternatives to the SWI methods employed here, are magnetization transfer (Helms et al., 2009) or proton density imaging (Deoni and Catani, 2007) techniques. The authors of the latter paper could determine the dentate nucleus at 3 T reliably on a group of 10 participants, and were also able to visualize the medial cerebellar nuclei in one individual after taking an average of 4 scans with an isotropic 0.7 mm resolution (total scan time 40 min). While a detailed comparison of different methods is beyond the scope of this paper, it would be interesting to determine which of the methods is best suited and most economical for high-field imaging.

Probabilistic atlas of the DCN

We summarized our results in a probabilistic atlas of the DCN. Because such atlases are dependent on the atlas template and normalization method, we generated these maps for SUIT normalization and the SPM segmentation and normalization algorithm. The latter provides very similar maps to those obtained with nonlinear alignment in FSL (FNIRT, Andersson et al., 2008). We have integrated the maps for the DCN with an existing probabilistic atlas for the human cerebellum, which contains 28 ROI for the different gray matter compartments (Diedrichsen et al., 2009). The atlas is made freely available (http://www.icn.ucl.ac.uk/motorcontrol/imaging/propatlas.htm) and can be viewed with FSL view (Smith et al., 2004), MriCroN (Rorden, 2007), and is also integrated into the SUIT toolbox for SPM. Although the data for the deep cerebellar nuclei comes from a separate set of participants than the data for the cerebellar lobules, we took great care that the normalization methods were comparable.

While the probabilistic maps for SPM segmentation/FNIRT normalization show slightly lower probabilities than for SUIT normalization, the atlases allow for each specific normalization method valid inferences about the likely origin of activity observed in fMRI group analyses.

The summary maps (Fig. 4), which show which structure a voxel most likely belonged to, can further be used to define region of interests for group analyses. The user, however, should keep in mind that this map is a thresholded probabilistic map. While location and overall extent of the structures in this summary map veridically reflect the average of the studied population, the shape and hence the volume of these structures are not necessarily representative. Thus, for detailed analysis this summary map should not be used as a substitute for ROIs based on the actual anatomy.

Group normalization for functional imaging of the DCN

The probabilistic maps also give us a measure of the remaining anatomical variability after spatial normalization. Using the best nonlinear normalization techniques currently available, the center of mass of each nucleus varied with a standard deviation of ~1.3–1.5 mm in each spatial direction. Because the deep cerebellar nuclei have a small volume, the average voxel in a group analysis within the dentate nucleus only reflects dentate activity in 1/3 of the participants, and 2/3 of the participants contributing activity from outside the dentate nucleus. This is especially problematic because the signal intensity on the EPI images – and therefore also the variability of the activation estimates – is substantially higher outside than inside the dentate nucleus. To make matters worse, motor and cognitive processes are likely to activate different subregions of the dentate nucleus (Dum and Strick, 2003). Thus, to interpret functional activation in a group fMRI study, normalization methods need not only to superimpose the DCN, but also to superimpose different compartments of these nuclei.

To improve the statistical power of the analysis of dentate activity, we have proposed here to draw a ROI that captures the bean-shaped hypo-intensity that indicates the location of the dentate and parts of the neighboring interposed nuclei. This can be done on a high-resolution T2*- or susceptibility-weighted image, or simply on the mean EPI image. While the EPI images provide a less clear picture of the dentate, the latter method has the advantage that possible image distortions are taken into account in the definition of the ROI.

One could now perform a standard ROI analysis across participants by averaging the activity across the whole ROI. While this technique would be adequate for information from fastigial and interposed nuclei, we would lose important spatial information within the dentate nucleus. Rather, we used here the ROI information in combination with the T1-weighted scan to superimpose both the dentate nuclei and the rest of the cerebellar structures. The combined normalization is performed in one automatic normalization step. Our results show that this technique indeed leads to a near perfect overlap of the dentate nuclei and also improves the overlap of interposed and fastigial nuclei, despite the fact that these were not part of the ROI which drove the normalization. The method combines the spatial specificity of ROI analyses and the information richness of map-wise approaches (for a debate between these two approaches see: Friston et al., 2006; Saxe et al., 2006).

While we yet have to compare this new normalization technique systematically using real functional data against other techniques, we believe that the small amount of extra work is justified by the gain in spatial specificity. Except the drawing of the ROIs, the normalization method is fully automatic and the Matlab code available as part of the SUIT toolbox for SPM (http://www.icn.ucl.ac.uk/motorcontrol/imaging/suit.htm).

Although the influence of different factors in such an analysis has not been fully explored, based on our current experience we would recommend the following analysis pipeline for the study of dentate activity: the within-subject 1st level analysis should be carried out in realigned, but otherwise unsmoothed and unnormalized fMRI time series data. Smoothing would be harmful at this point, as the T2* signal surrounding the DCN is much higher than in the DCN itself. After drawing the ROIs, one would then mask the coefficient-images from each participant with the dentate ROI. The masking prevents that signal within the dentate nucleus is averaged through smoothing with the noisier signal from surrounding regions. The images are then normalized to the SUIT template and the dentate template to bring them into the atlas space. We recommend the use of a minimal smoothing kernel that matches the size of the functional units in the dentate nucleus (2–3 mm FWHM). For inference on the group level, a correction for multiple tests needs to be performed. Because of the small volume and the lack of spatial smoothness, the application of random-field theory (Friston et al., 1994; Worsley et al., 1996) would not be valid. We therefore recommend permutation methods (Nichols and Hayasaka, 2003; Nichols and Holmes, 2002), taking advantage of their minimal assumptions and robustness. Using these techniques, functional imaging of the deep cerebellar nuclei in humans should become more sensitive, without sacrificing specificity. While the techniques described here were developed for the imaging of the DCN, the same methods are applicable for functional imaging of any nuclear structure that can be visualized using MRI.

Acknowledgments

References

Andersson, J.L., Smith, S.M., Jenkinson, M., 2008. FNIRT — FMRIB's non-linear image registration tool. Organ. Hum. Brain Mapp.

Angevine, J.B., Mancall, E.L., Yakovlev, P.I., 1961. The human cerebellum. An atlas of Gross Topography in Serial Sections. Little, Brown and Company, Boston.

Aoki, S., Okada, Y., Nishimura, K., Barkovich, A.J., Kjos, B.O., Brasch, R.C., Norman, D., 1989. Normal deposition of brain iron in childhood and adolescence: MR imaging at 1.5 T. Radiology 172, 381–385.

Ashburner, J., Friston, K.J., 2005. Unified segmentation. Neuroimage 26, 839–851.

Blinkov, S., Glezer, I., 1968. The human brain in figures and tables. A Quantitative Handbook. Plenum, New York.

Chan-Palay, V., 1977. Cerebellar dentate nucleus. Organization, Cytology, and Transmitters. Springer Verlag, Berlin.

Dejerine, J., 1901. Anatomie des Centres Nerveux. II. J. Rueff, Paris.

Deoni, S.C., Catani, M., 2007. Visualization of the deep cerebellar nuclei using quantitative T1 and rho magnetic resonance imaging at 3 Tesla. Neuroimage 37, 1260–1266.

Diedrichsen, J., 2006. A spatially unbiased atlas template of the human cerebellum. Neuroimage 33, 127–138.

Diedrichsen, J., Balsters, J.H., Flavell, J., Cussans, E., Ramnani, N., 2009. A probabilistic MR atlas of the human cerebellum. Neuroimage 46, 39–46.

Diedrichsen, J., Shadmehr, R., 2005. Detecting and adjusting for artifacts in fMRI time series data. Neuroimage 27, 624–634.

Dimitrova, A., de Greiff, A., Schoch, B., Gerwig, M., Frings, M., Gizewski, E.R., Timmann, D., 2006a. Activation of cerebellar nuclei comparing finger, foot and tongue movements as revealed by fMRI. Brain Res. Bull. 71, 233–241.

Dimitrova, A., Weber, J., Redies, C., Kindsvater, K., Maschke, M., Kolb, F.P., Forsting, M., Diener, H.C., Timmann, D., 2002. MRI atlas of the human cerebellar nuclei. Neuroimage 17, 240–255.

Dimitrova, A., Zeljko, D., Schwarze, F., Maschke, M., Gerwig, M., Frings, M., Beck, A., Aurich, V., Forsting, M., Timmann, D., 2006b. Probabilistic 3D MRI atlas of the human cerebellar dentate/interposed nuclei. Neuroimage 30, 12–25.

Dum, R.P., Strick, P.L., 2003. An unfolded map of the cerebellar dentate nucleus and its projections to the cerebral cortex. J. Neurophysiol. 89, 634–639.

Duvernoy, H.M., 1995. The human brain stem and cerebellum. Surface, Structure, Vascularization, and Three-dimensional Sectional Anatomy with MRI. Springer-Verlag, Wien.

Friston, K., Holmes, A.P., Ashburner, J., 1999. Statistical parameter mapping (SPM).

Friston, K.J., Rotshtein, P., Geng, J.J., Sterzer, P., Henson, R.N., 2006. A critique of functional localisers. Neuroimage 30, 1077–1087.

Friston, K.J., Worsley, K.J., Frackowiak, R.S.J., Mazziotta, J.C., Evans, A.C., 1994. Assessing the significance of focal activations using their spatial extent. Hum. Brain Mapp. 1, 214–220.

Gans, A., 1924. Beitrag zur Kenntnis des Aufbaus des Nucleus dentatus aus zwei Teilen, namentlich auf Grund von Untersuchungen der Eisenreaktion. Z. ges. Neurol. Psychiatr. 93, 750–755.

Gizewski, E.R., de Greiff, A., Maderwald, S., Timmann, D., Forsting, M., Ladd, M.E., 2007. fMRI at 7 T: whole-brain coverage and signal advantages even infratentorially? Neuroimage 37, 761–768.

Guizzetti, P., 1915. Principali risultati dell'applicazione grossolana a fresco delle reazioni istochimiche del ferro sul sistema nervoso centrale dell'uomo e di alcuni mammiferi domestici. Riv. di patologia nervosa e mentale 20.

Haacke, E.M., Mittal, S., Wu, Z., Neelavalli, J., Cheng, Y.C., 2009. Susceptibility-weighted imaging: technical aspects and clinical applications, part 1. AJNR Am. J. Neuroradiol. 30, 19–30.

Haacke, E.M., Xu, Y., Cheng, Y.C., Reichenbach, J.R., 2004. Susceptibility weighted imaging (SWI). Magn. Reson. Med. 52, 612–618.

Habas, C., 2009. Functional imaging of the deep cerebellar nuclei: a review. Cerebellum 9, 22–28.

Heimburger, R.F., Whitlock, C.C., 1965. Stereotaxic destruction of the human dentate nucleus. Confin. Neurol. 1965, 346–358.

Helms, G., Draganski, B., Frackowiak, R., Ashburner, J., Weiskopf, N., 2009. Improved segmentation of deep brain grey matter structures using magnetization transfer (MT) parameter maps. Neuroimage 47, 194–198.

Höpker, W., 1951. Das altern des nucleus dentatus. Z. Altersforschung 5, 256–277.

Jakob, A., 1928. Das Kleinhirn. Möllendorfs Handbuch der mikroskopischen Anatomie des Menschen. Springer Verlag, Berlin, pp. 674–916.

Jansen, J., Brodal, A., 1958. Das Kleinhirn. In: Möllendorff, W.V., Bargmann, W. (Eds.), Handbuch der mikroskopischen Anatomie des Menschen. Springer Verlag, Berlin Göttingen Heidelberg, pp. 1–323.

Kim, S.G., Ugurbil, K., Strick, P.L., 1994. Activation of a cerebellar output nucleus during cognitive processing. Science 265, 949–951.

Kozlova, G.P., 1984. Individual anatomical variations in cerebellar nuclei. Neurosci. Behav. Physiol. 14, 63–67.

Küper, M., Dimitrova, A., Maderwald, S., Elles, H.G., Gizewski, E.R., Diedrichsen, J., Timmann, D., under review. Evidence for a motor and a non-motor domain in the human dentate nucleus — an fMRI study.

Larsell, O., Jansen, J., 1972. The comparative anatomy and histology of the cerebellum. The Human Cerebellum, Cerebellar Connections and Cerebellar Cortex. The University of Minnesota Press, Minneapolis.

Maschke, M., Weber, J., Dimitrova, A., Bonnet, U., Bohrenkamper, J., Sturm, S., Kindsvater, K., Muller, B.W., Gaspar, M., Diener, H.C., Forsting, M., Timmann, D., 2004. Age-related changes of the dentate nuclei in normal adults as revealed by 3D fast low angle shot (FLASH) echo sequence magnetic resonance imaging. J. Neurol. 251, 740–746.

Middleton, F.A., Strick, P.L., 1997. Cerebellar output channels. In: Schahmann, J.D. (Ed.), The Cerebellum and Cognition. Academic Press, San Diego, CA, pp. 31–60.

Nichols, T., Hayasaka, S., 2003. Controlling the familywise error rate in functional neuroimaging: a comparative review. Stat. Meth. Med. Res. 12, 419–446.

Nichols, T.E., Holmes, A.P., 2002. Nonparametric permutation tests for functional neuroimaging: a primer with examples. Hum. Brain Mapp. 15, 1–25.

Oldfield, R.C., 1971. The assessment and analysis of handedness: the Edinburgh inventory. Neuropsychologia 9, 97–113.

Rorden, C., 2007. MRICroN.

Saxe, R., Brett, M., Kanwisher, N., 2006. Divide and conquer: a defense of functional localizers. Neuroimage 30, 1088–1096 (discussion 1097–1089).

Schmahmann, J.D., Doyon, J., Toga, A., Petrides, M., Evans, A., 2000. MRI Atlas of the Human Cerebellum. Academic Press, San Diego.

Smith, S.M., Jenkinson, M., Woolrich, M.W., Beckmann, C.F., Behrens, T.E., Johansen-Berg, H., Bannister, P.R., De Luca, M., Drobnjak, I., Flitney, D.E., Niazy, R.K., Saunders, J., Vickers, J., Zhang, Y., De Stefano, N., Brady, J.M., Matthews, P.M., 2004. Advances in functional and structural MR image analysis and implementation as FSL. Neuroimage 23 (Suppl 1), S208–S219.

Stoodley, C.J., Schmahmann, J.D., 2009. Functional topography in the human cerebellum: a meta-analysis of neuroimaging studies. Neuroimage 44, 489–501.

Thomsen, K., Piilgaard, H., Gjedde, A., Bonvento, G., Lauritzen, M., 2009. Principal cell spiking, postsynaptic excitation, and oxygen consumption in the rat cerebellar cortex. J. Neurophysiol. 102, 1503–1512.

Timmann, D., Brandauer, B., Hermsdörfer, J., Ilg, W., Konczak, J., Gerwig, M., Gizewski, E.R., Schoch, B., 2008. Lesion-symptom mapping of the human cerebellum. Cerebellum 7, 602–606.

Voogd, J., 2004. Cerebellum and precerebellar nuclei. In: Paxinos, G., Mai, J. (Eds.), Human Nervous System. Elsevier, pp. 321–392.

Worsley, K.J., Marrett, S., Neelin, P., Vandal, A.C., Friston, K.J., Evans, A.C., 1996. A unified statistical approach for determining significant voxels in images of cerebral activation. Hum. Brain Mapp. 12, 900–918.